Development of an anthropomorphic breathing phantom for proton therapy verification

SEMESTER PROJECT

D-ITET, FS 2017

Patrick Bosshard

May 2017

Supervisor: Prof. Dr. Anthony Lomax
Advisors: Dr. Giovanni Fattori
Dr. Rosalind Perrin

Abstract

Anthropomorphic phantoms are valuable tools for verification and validation purposes in radiotherapy. This study reports first steps in the development of a target decoupling system and vessel-like structures within the lung compartment of an already existing lung phantom. A set-up that induces motion of a motor as a function of the pressure within the phantom was built up. By using an optical tracking system the latency between phantom motion and motor motion was determined to 77.67 ± 17.52 ms. A 3D printed rubber-like lung structure was examined using 4D CT and image registration. Tracking resp. motion field analysis of the artificial vessels showed -3.3 ± 0.4 mm resp. -3.3 ± 0.3 mm motion in anterior-posterior direction and 1.5 ± 0.4 mm resp. 1.6 ± 0.3 mm in superior-inferior direction. The registration suggests more realistic motion fields compared to the featureless lung phantoms.

Table of Contents

1 Introduction

In order to treat cancer, radiotherapy plays an important role alongside surgery and chemotherapy. In radiotherapy, photons or charged particles are used to irradiate tumors while sparing the surrounding normal tissue. In addition, the tumor should receive the same dose throughout its volume without any hot or cold spots. This can be problematic when facing real patients.

1.1 Motion

The real patient is a moving and inhomogeneous object. One can differentiate motion between treatment sessions (inter-fractional motion) and motion within treatment sessions (intra-fractional motion). This report focuses mainly on intra-fractional motion. Target motion can lead to unwanted deviations of the actual dose distribution from the planned dose distribution, for example, blurring out of the dose gradient [1]. In addition changes in the radiological path length can also occur due to motion of organs into the beam path [2]. Another problem can be the loss of dose uniformity due to inference when using beam scanning methods [3].

Special motion-mitigation techniques can deal with this problem. But, in order to validate and verify such methods, dedicated phantoms are needed to mimic the motion of real patients.

1.2 Lung phantom

One reason for intra-fractional target motion is breathing. The filling and emptying of the lung with air causes motion in the whole thorax. The Paul Scherrer Institute (PSI) in Villigen, Switzerland developed a lung phantom which is capable of mimicking the motion caused by the breathing [4]. It consists of an inflatable lung with ribs and skin. A target with radiochromic films can be inserted into the lung phantom. A pumping system is able to apply different breathing cycles by pumping air in and out, which causes the target to move. This set-up can be used to study the influence of breathing on the thorax and, in particular, on the target.

However, in this particular phantom the target will always move in phase with the rest of the thorax. Since patient thorax and tumour motion are not always in phase, one may want to simulate situations in the phantom in which the target and the lung are moving out of phase. For mimicking such motions a decoupling of the target and the thorax motion is required. Another limitation of the phantom is the featureless lung. Real lungs have many structures inside their volume coming from the veins, arteries and the bronchial tree. For more realistic measurements additional structures have to be implemented into the lung.

Aim of the project: The project aims to develop the already existing lung phantom further by decoupling the target motion from the thorax motion and by providing more realistic lung structures. The target motion decoupling should be achieved by measuring the pressure and setting the target into motion with the help of a motor. In a second step the lung compartment should be modified by adding more realistic lung structures. The structure should be made of a material, which is flexible enough to move during inflation and deflation in order to perform deformable image registration.

2 Standalone motion controller

At the current stage of development, the motion of anatomical structures forming the thorax and the internal tumour model of Lung Cancer (LuCa) breathing phantom are strictly linked. As inlet air pressure is the only driving force, it is not possible to model realistic internal-external correlation patterns observed in patients, typically characterized by shifts in phase and baseline over time. An independent motion controller for the tumour model, although increasing the setup complexity, opens to the experimental simulation of more realistic motion scenarios, to support research activities in the field of motion mitigation techniques.

The project concept is shown in Fig. 1 and consists of developing a motion controller that starting from the measured lung pressure, controls the target motion with a generic transfer function that can be extended arbitrarily by the user.

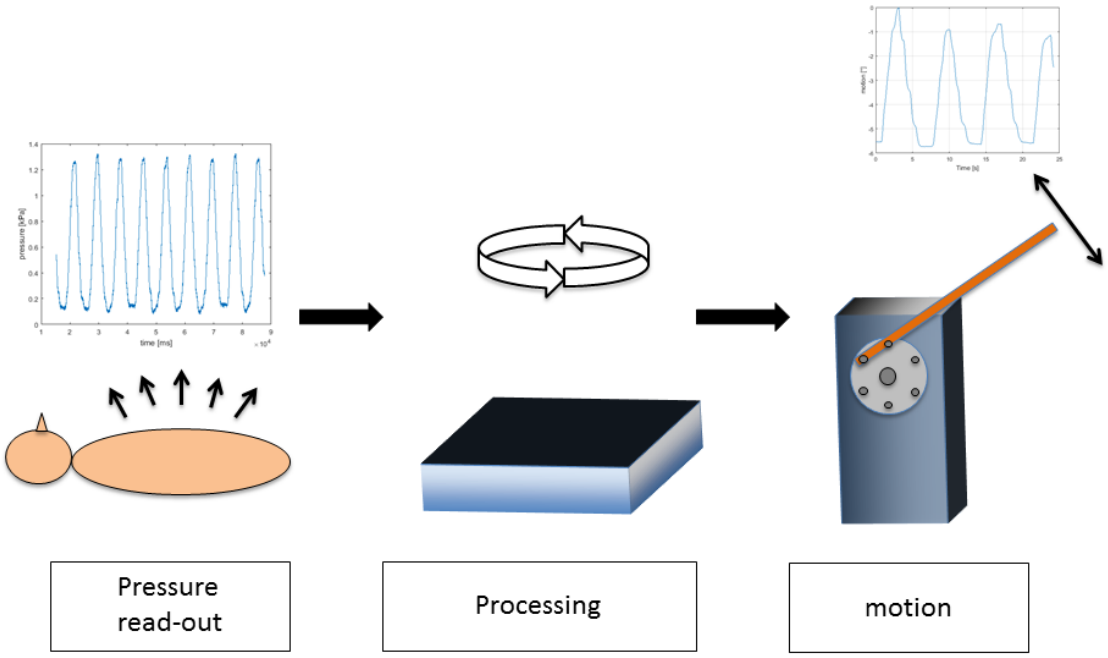

Fig. 1: Concept of a standalone motion controller for LuCa phantom target

2.1 Controller development

The standalone motion controller consists of four main components that are listed below and briefly described in the following paragraphs:

- Microcontroller processing unit (Section 2.1.1)
- Pressure sensor (Section 2.1.2)
- Motion actuator (Section 2.1.3)
- Processing logic (Section 2.1.4)

2.1.1 Arduino breakout board

The used Arduino breakout board has 20 digital in- and outputs. Six of them can be used as analog inputs. The digital in- and outputs and the analog input can be configured to use either 3.3 V or 5 V. The pins 0 (RX) and 1 (TX) can be used for serial communication (UART). In addition the board is also compatible with standard Arduino plug-in shields (designed for Arduino Uno R3). The board provides also an integrated micro SD card reader [5].

2.1.2 Pressure sensor

The pressure sensor is the ADP51B63 from Panasonic [6]. From datasheet, the component has 0 kPa to 6 kPa rated pressure range relative to ambient. Signal amplification and temperature compensation is built-in, therefore no additional conditioning circuit is required.

The schematic of the sensor pinning and interface to Arduino is shown in Fig. 2. The pins V_{cc} (power supply 5V), GND (ground) and V_{out} (output voltage) of the sensor are connected to the appropriate pins of the microcontroller (Intel® Edison Arduino Breakout). A 1 µF and a 0.01 µF capacitor are placed between the V_{cc} and the GND according to the datasheet. The V_{out} pin delivers the signal to the analog input of the Arduino board where the data are quantized.

The measured signal can be converted into the applied pressure by using the transfer function from the datasheet (Fig. 3) [6].

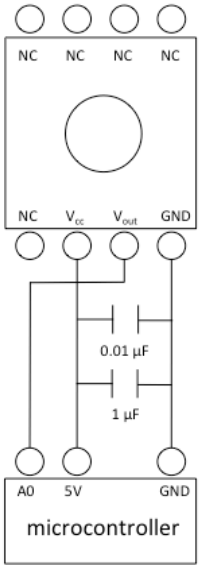

Fig. 2: Schematic of the pressure sensor pinning and connection to microcontroller. The pins (small circles) V_{cc} (power supply 5V), GND (ground) and V_{out} (output voltage) of the sensor are connected to the corresponding microcontroller (Arduino) pins A0 (analog input), 5 V and GND. In addition two capacitors (1 µF and 0.01 µF) are placed between the V_{cc} and the GND, NC = not used.

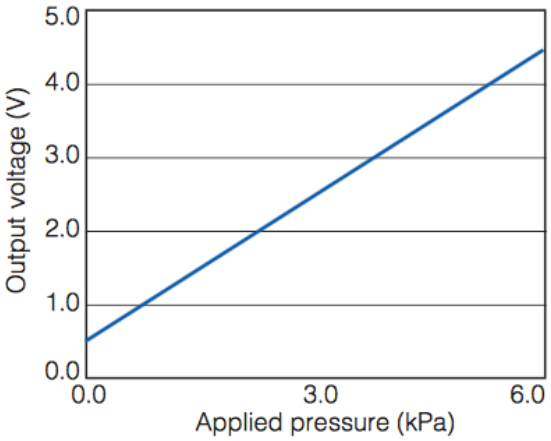

Fig. 3: Transfer function: Relationship between the output voltage and the applied pressure of pressure sensor [6]

2.1.3 Motor

The technical requirement specifications for the actuator are the following:

- Smooth motion
- Long operating time (1h continuous motion), no duty cycle constraints.
- Reasonable purchase cost: below 500 Eur.
- If possible: closed-loop feedback system

Many different types of actuators are available on the market, whose characteristics are briefly discussed in the following.

- Pneumatic & hydraulic motor:
    - Pneumatic motors generate mechanical work by expanding compressed air. Hydraulic motors use the same principle but the air is replaced by an incompressible liquid. They are able to produce very smooth motions, but leakage might occur and require sophisticated calibration procedures to accurately control the motion [7].

- Stepper motor:
    - Stepper motors use electrical power to move and divide a full 360 degrees rotation in small steps. Budget devices typically implement rather large step size (1.8°) that makes smooth and continuous motion modulation difficult to achieve. Moreover, closed loop is generally left to user, to be implemented in the control loop code [8].

- Servo motor:
    - Servo motors combine an electrical motor, a position sensor and a closed-loop control in one piece of equipment. Given a positional set point and speed, the build-in controller automates the power modulation to reach/maintain accurately the desired shaft position as function of the load applied on the end effector [8].

Based on the technology review, servo motors fulfil the project requirements and, thanks to built-in closed loop control, substantially ease the development effort. Among the available off-the-shelf products, we selected the Dynamixel MX-28R from Robotis (Lake Forest, CA, US) [9, 10], a "smart" servo actuator primarily designed for robotics. Unlike many similar products that use potentiometers to retrieve the shaft position, MX-28 serie devices rely on a magnetic encoder within the closed-loop control, for reliable set point reproducibility and positional accuracy. Moreover, the very fine angular resolution (0.088°) facilitates smooth sinusoidal drives, required to reproduce respiratory motion traces.

With reference to Fig. 4, the communication between Arduino and the MX-28R is handled by the UART to RS485 transceiver MAX485, from Maxim Integrated (San Jose, CA, US)

[11]. The module is powered with 5 V supply from the Arduino, wired with a 2.2 µF protection capacitor. Besides RX and TX signal lines, the half-duplex communication direction is controlled by a digital output (D5 in Fig. 4) on the Arduino breakout board.

The concept of this setup has already been proven effective in the Smart Grasp project form Walter Bircher and Mike Leddy [12].

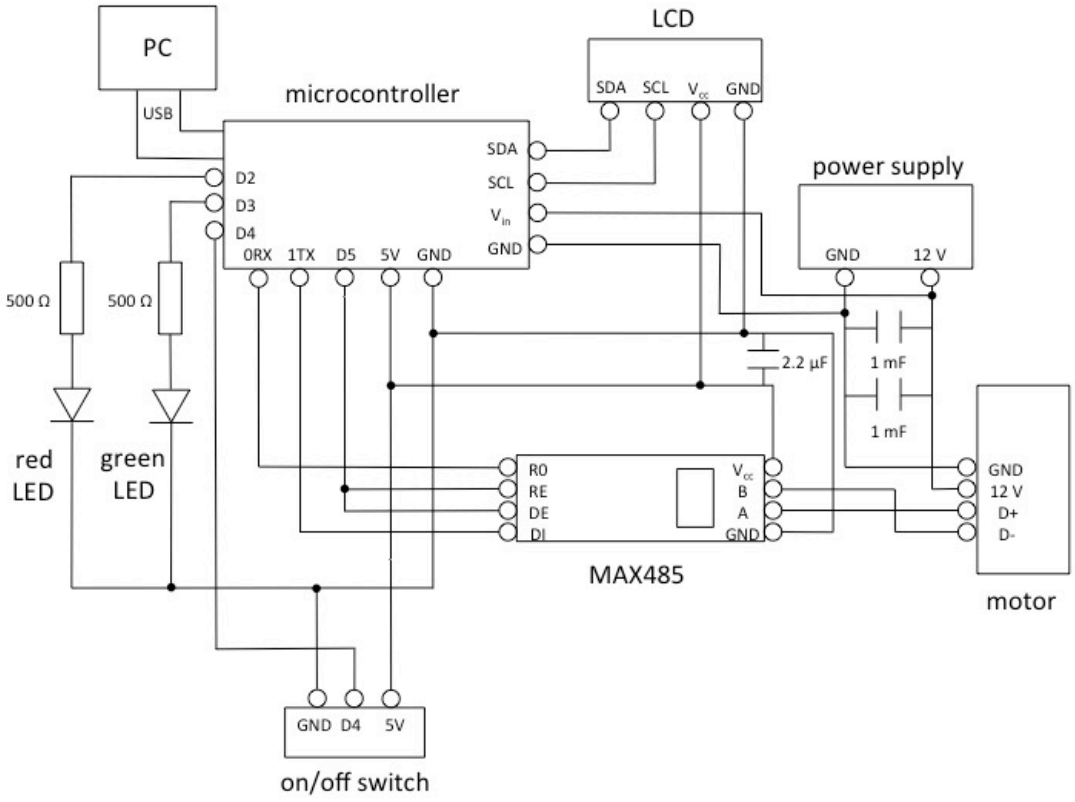

Fig. 4: Schematic of motor wiring. The connections between the PC, microcontroller, LCD, LEDs, on/off switch, power supply, MAX485 module and motor are shown by black lines. Black dots represent connections of crossing lines.

Even though an application programming interface (API) is not officially released by Robotis, few examples can be found online. For instance, Dynamixel_Serial [13] library implements Arduino compatible C API to handle serial communication with MX serie motor models. With the purpose of speeding up the development process, instead of writing a new interface from scratch, Dynamixel_Serial library has been revised to support our specific motor type and reduce communication latencies.

All the connection seen in Fig. 2 and Fig. 4 were implemented on a plug-in shield, which fits standard Arduino pinning scheme (Fig. 5).

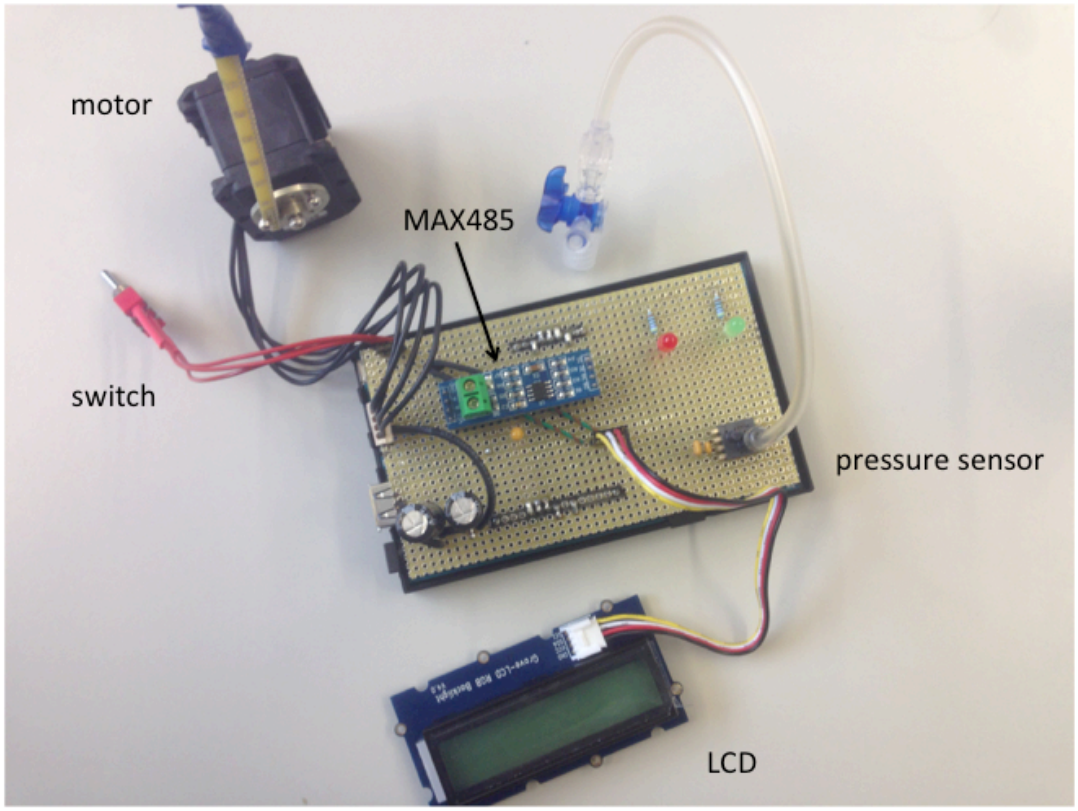

Fig. 5: Plug-in shield on Arduino board with motor, LCD, pressure sensor, on/off switch and MAX458 module

2.1.4 Processing

The analogic pressure signal quantized by the Arduino ADC is processed to obtain pressure values. 10-bit digital levels are converted to mbar as follows:

$$pressure = \frac{\frac{analog\ signal \cdot \text{max.}\ voltage}{1023} - 0.5\ V}{4\ V} \cdot 60\ mbar \tag{1}$$

where max. voltage equals 5 V.

Once computed, the pressure value is compared with safety boundaries set by the sensor producer to trigger measurement interlock and activate a red alarm LED (Fig. 4).

Eventually, the motor angular set point is obtained from the analog signal by applying a simple linear proportion:

$$position = analog\ signal \cdot \frac{512}{1023} + (2048 - 256) \tag{2}$$

The motion range of the motor is 45 degrees (512*0.088°=45.056°). The last term of equation (2) represents the zero point of the position (can be choosen arbitrarily), where 2048 is the center position (180°) of the overall possible motion (0 to 4095). In addition the user can set gain and offset parameters to further modify the position. It is implemented as follows:

If position > 2048:

$$position_{new} = (position - 2048) \cdot gain + 2048 + offset \quad (3)$$

And if position ≤ 2048:

$$position_{new} = -(2048 - position) \cdot gain + 2048 + offset \quad (4)$$

Speed modulation is applied to preserve motion smoothness over a wide range of characteristics of input pressure signal. Specifically, the first derivative of the pressure trace is computed and used to proportionally correct the motor's shaft rotating speed.

The first derivative was calculated by saving pressure values and time stamps in a buffer (buffer length can be specified by the user) and apply the least square algorithm to calculate the derivation. Each time new values are measured the buffer is updated accordingly.

User interaction and status feedback

An on/off switch enables the motion of the motor and the data logging by generating a new file. The current state of the switch can be seen by a green LED (light on means switch is on) (Fig. 4).

An LCD display is updated in real time to provide the user with visual feedback about current sensor voltage and pressure value. The display is produced by Seeed Technology Inc. [14] and uses I2C communication protocol. Connection with Arduino required standard V_{cc}, GND, SDA (Serial Data Access) and SCL (Serial Clock) lines (Fig. 4).

Data logging

Measured pressure and milliseconds timestamp are saved on the micro SD card embedded on the Arduino breakout board. To limit file write access, the data are buffered and flushed to the file at 1 Hz.

2.2 Experimental validation of the motion controller

2.2.1 Experimental set-up and data processing

The developed controller has been tested operating the respiratory phantom under different motion conditions, to assess the actuation latency. Each measurement has been repeated setting different gain and angular motion range (Table 1).

As shown in Fig. 6, the pressure sensor can be connected to a silicon derivation tube hand-crafted on the standard LuCa ventilation pipe, to measure the total pressure resulting of static and dynamic components in the air inlet pipe. For convenience, a small cantilever has been solidly fixed on the motor shaft to ease the observation of motion output.

Optical tracking (Polaris Spectra from NDI) was applied to simultaneously measure the lung surface motion resulting of jet ventilation and the motor shaft rotation. For this purpose, two infrared coated markers were fixed on the lung surface and the motor shaft cantilever tip (Fig. 7).

A clinically relevant range of pressure curves was applied (Table 1) including sinusoidal and patient wave curves.

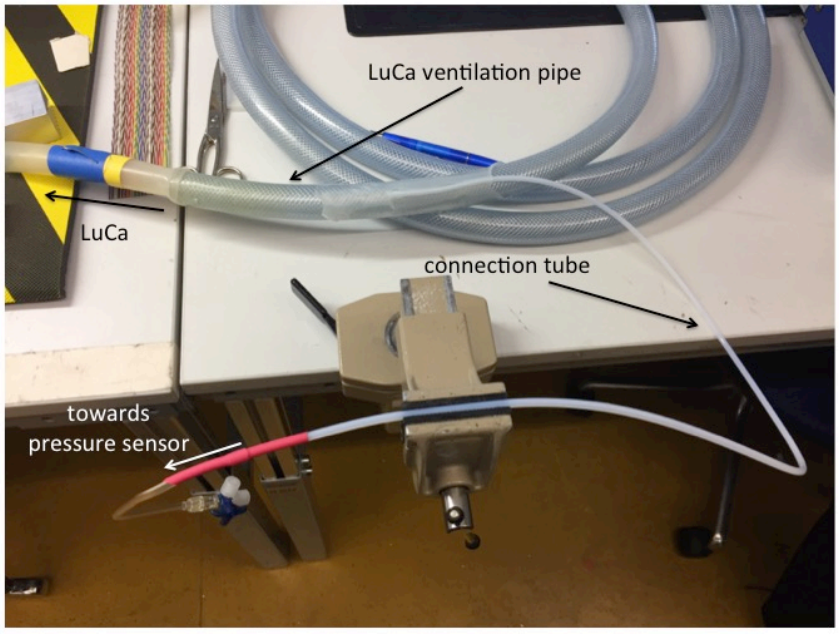

Fig. 6: Connection tube between pressure sensor and LuCa ventilation pipe

Table 1: Different breathing cycles for motion tracking measurements (patient data filename: patient_S18_Yepmax12_pmin8_180s)

	Ventilation system				Motor	
No.	**Curve type**	**Period**	**Gain**	**Offset**	**Angular range**	**Gain**
1	$\sin^4$	4s	18	3	45°	1
2	$\sin^4$	4s	18	3	45°	2
3	$\sin^4$	4s	18	3	90°	1
4	$\sin^4$	4s	18	3	90°	2
5	patient	-	1	10	45°	1
6	patient	-	1	10	45°	2
7	$\sin^4$	8s	18	3	45°	1
8	$\sin^4$	8s	18	3	45°	2

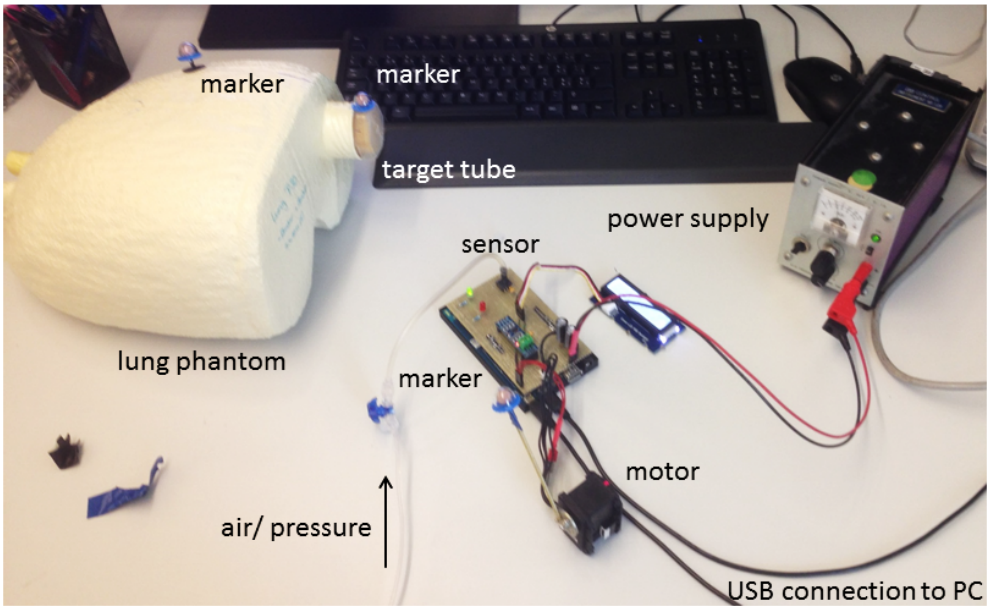

Fig. 7: Microcontroller and motor setup connected to a power supply, computer and the lung phantom. Markers for optical tracking were placed on a stick fixed at the motor and on the lung phantom.

The delay between the lung surface and the motor is estimated applying a model-based approach:

1. The 3D coordinates of the marker fixed on the tip of the *motor* shaft are transformed from Cartesian to polar reference system.

2. The *motor* signal and the lung *surface* trace are smoothed using Savitzky-Golay filtering and resampled on a common time grid with 10 ms sample period.
3. Fourier transform is applied to estimate the phase corresponding to the fundamental frequency of *motor* and *surface* signals.
4. The phase difference is provided as a measure of signal jitter, quantifying the latency between *surface* and *motor* motion.

This approach could not be applied to patient breathing curves, due to their non-stationary nature and, therefore, the jitter analysis is based solely on sinusoidal motion data.

2.2.2 Results

Exemplary motion traces for both surface and target motion are shown in Fig. 8.

The obtained delays and total angular range motion of the motor for the different breathing cycles are listed in Table 2. As already mentioned, the Fourier analysis could not be applied to patient breathing waveforms, due their non-stationary nature. On average the measured latency is 77.67 ± 17.52 ms. When comparing two measurements of the same curve type and angular range, the latency is inversely proportional to the gain.

Table 2: Different applied breathing cycles and their parameters with the delays between the surface motion and the motor motion and the total angular motion of the motor.

No.	Curve type	Range of degrees	Gain	Delay	Total angular motion
1	$\sin^4$, T = 4s	45°	1	93.8 ms	4.78°
2	$\sin^4$, T = 4s	45°	2	80.0 ms	12.46°
3	$\sin^4$, T = 4s	90°	1	80.8 ms	12.01°
4	$\sin^4$, T = 4s	90°	2	73.5 ms	29.54°
5	patient	45°	1	-	5.72°
6	patient	45°	2	-	13.28°
7	$\sin^4$, T = 8s	45°	1	92.3 ms	6.00°
8	$\sin^4$, T = 8s	45°	2	45.6 ms	11.93°

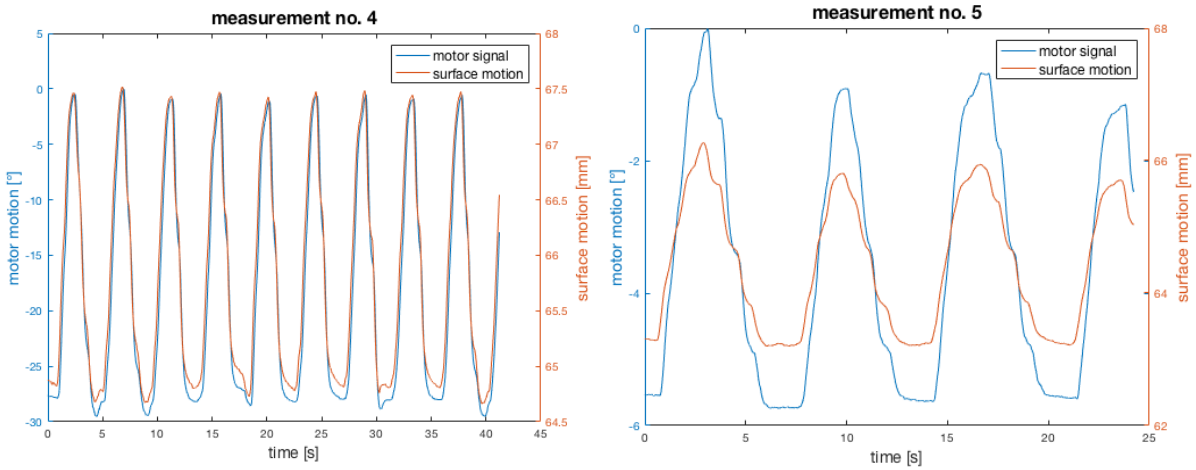

Fig. 8: Motor motion vs. surface motion: Left graph: measurement no. 4, right graph: measurement no. 5, blue curve: Transformed and resampled motor motion in degrees vs. time (left y-axis), red curve: Resampled surface motion in mm vs. time (right y-axis).

In addition, the sampling rate of the developed motion controller has been evaluated analysing pressure sample timestamps in the system log files. Overall, the sampling period was 8.67 ± 1.15 ms, consisting of an average sampling frequency of ~115Hz.

2.2.3 Discussion

The developed motion controller has been tested in experimental settings to quantify the actuation latency.

Hereafter, the main components contributing to 77.67 ± 17.52 ms delay between the motion of the phantom surface and the target are listed and briefly discussed:

i. *Propagation time of the pressure waveform in the measurement probe*
   A simple approximation considering 340 m/s as the pressure velocity in air, gives approx. 10 ms delay due to the waveform propagation along the measurement probe tube length. Moreover, the probe pipe is made out of silicon, therefore the dumping effect due to material elasticity might increase the measurement latency.
ii. *Computational time required to derive motor set points from pressure data.*
   Based on the analysis of pressure samples' timestamps, the processing time is 8.67 ± 1.15 ms.
iii. *Communication delay*
   The communication between Arduino board and motor is half-duplex and relies on a UART-to-RS transceiver. Depending on the message length, the data exchange

requires a variable amount of time. The communication time hasn't been investigated within this project.

iv. *Motor response time and discretization of motor shaft positions*

The motor has its own response time. Moreover, depending on the gain parameter setting, small pressure changes might be mapped to same shaft position, resulting in skipped motor command per pressure sample.

v. *Inherent mechanical dynamic of the phantom*

The latency value brought to the reader is based on the comparison between the observed lung expansion and motor shaft rotation. The surface displacement is however just the result lung's material stretching that follows a pressure variation. Therefore, the mechanical properties of the material when subject to dynamic forces affect the quantified latency.

3 Development of lung structures

An artificial lung structure was generated using 3D printing and examined in regard to motion during pressurisation of the phantom. In addition the influence on deformable image registration was investigated.

3.1 Preparation & 3D printing

A 3D model of the bronchial tree was generated using the software Slicer and the „Vascular Modeling Toolkit“-extension (VMT). CT volumes were loaded into Slicer and cropped such that just the left part of the lung remained. Afterwards branching structures of the bronchial tree were extracted from the CT volume by using the function “Vesselness Filtering” from the VMT extension by placing a fiducial marker near the splitting of the bronchus into the left and right lungs. The vessels were labelled and unnecessary structures such as the ribcage and other artefacts manifesting themselves as islands were removed. The obtained label map was used to generate a model for 3D printing (STL file format) (Fig. 9, A).

First, a part of the lung structure was printed on the PSI Reprographics department’s “Mark Two” printer with nylon (density 30%). The printing process was terminated before finishing, because of printing failures. Nevertheless a small structure was printed out with some vessel structures (Fig. 9, B). The structure was not very flexible and would probably not have provided a lot of motion in the lung phantom.

Next the whole lung model was printed with VisiJet M2 EBK (flexible, rubber-like material) at the company Steiner 3D (part of Steiner Werkzeugmaschinen AG) using a ProJet MJP 2500 printer. For more detailed information regarding the material the reader is referred to the datasheet of VisiJet M2 Materials from 3D SYSTEMS [15] (Fig. 9, C). The printed structure was very flexible compared to the nylon structure. The flexibility was almost too high, such that the structure could not maintain its form and looked flat after a while. Nevertheless the structure was used for further investigation because it was suitable to be inserted into the lung phantom and due to its flexibility would potentially move during inflation and deflation.

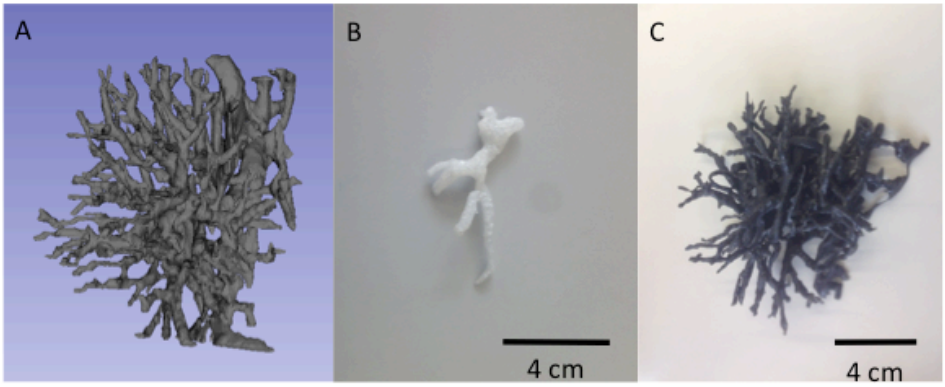

Fig. 9: Model and 3D printed lungs: A: modelled lung structure, B: 3D print of part of the lung structure made of nylon, C: 3D print of the lung structure made of VisiJet M2 EBK

3.2 Examination of the lung structure

3.2.1 Displacement analysis & qualitative comparison of image registration

A small piece of the lung structure made of VisiJet M2 EBK was cut out and inserted into the lung phantom (in between two layers of the foam inside the lung). A 4D CT was done using the ventilation system ($\sin^4$, T = 4s, gain = 50, offset = -25) and a respiratory gating system to measure the inhalation and exhalation (AZ-733V from Anzai Medical). The pressure was oscillating between -25 mbar and 25 mbar. After the acquisition 14 different phases in the respiratory cycle were reconstructed (Fig. 10).

Fig. 10: Phantom set-up for 4D CT and phase assignment: (A): phantom placed on a treatment table, left: tube connected to the ventilation system, right: belt with load cell for respiration measurement, (B): display for phase assignment, lower part shows the breathing cycle and the grey squares represent the same phase.

The data was recorded and movements of the lung vessels were tracked in 2D using a Matlab code provided by Dr. Rosalind Perrin (PSI). The code allows for selection of structures and tracking the displacement of the centroid of the structure in the sagittal plane

over all recorded phases. Five different vessels were tracked over the 14 phases and their displacements in regard to the first phase were examined.

In the next step, deformable image registration was applied on the reconstructed data using plastimatch (www.plastimatch.org). The first respiratory phase was considered as the non-moving image. All other phases were registered in respect to the non-moving image. The registration was done using the parameter sets first developed by Christos Bikis in his Semester Project (Thesis provided by Dr. Rosalind Perrin (PSI)) [16].

The registration led to motion fields, which were examined to estimate the motion of the vessels in 3D by choosing the same coordinates (the same vessels) as for the vessel tracking done in the first step. Afterwards, the displacements from the vessel tracking in the sagittal plane and the displacements from the motion fields were compared.

To investigate the influence of the lung structure on the image registration additional 4D CTs were acquired (same parameters as above). The acquisition was done once without and once with the lung structure. The registration between the 0% IN (inhalation) phase and the 100% IN phase of each 4DCT was performed using the same parameters as above. The results of the registration were qualitatively compared considering the motion field using the software VV.

3.2.2 Results

The motion of the vessels was displayed in phase vs. displacement plots for anterior-posterior motion and superior-inferior motion for 2D vessel tracking and deformation field analysis (Fig. 11). The first phase indicates the start of the inhalation and 14^{th} phase the end of the exhalation. As expected the start of inhalation and the end of exhalation showed similar displacements (for the 2D tracking as well as for the motion field analysis). The maximum motion averaged over the five vessels in anterior-posterior direction was -3.3 ± 0.4 mm and -3.3 ± 0.3 mm for the 2D tracking and the deformation field analysis respectively, and in superior-inferior direction 1.5 ± 0.4 mm and 1.6 ± 0.3 mm respectively. The average difference in maximum displacement between the two measurements for the same vessel is 0.2 ± 0.1 mm in anterior-posterior direction and 0.2 ± 0.1 mm in superior-inferior direction. Both methods showed similar displacements in the order of millimeters.

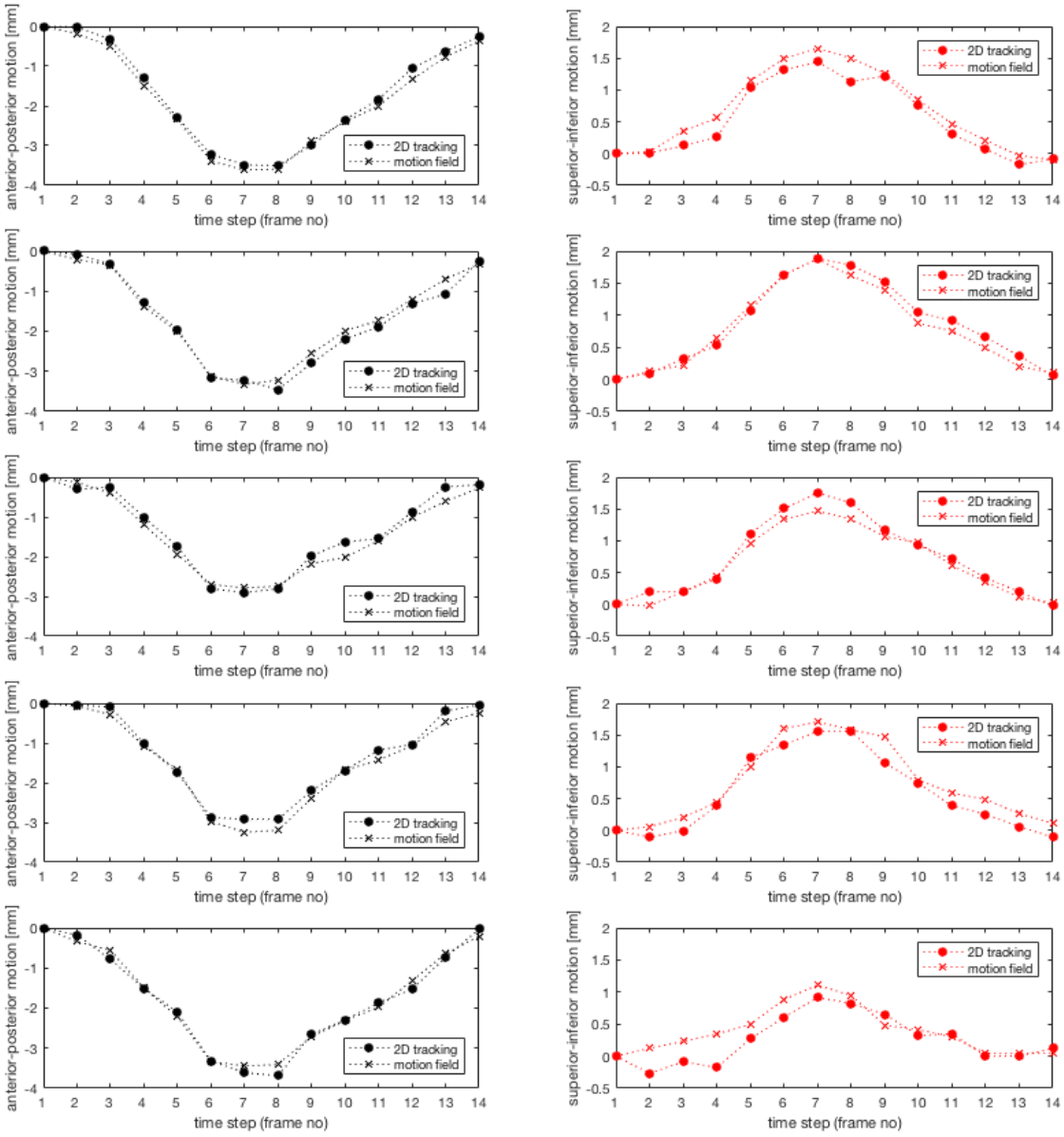

Fig. 11: Phase vs. displacement, left column: displacement in anterior-posterior direction, right column: displacement in superior-inferior direction, each row represents one vessel (coordinates according to vv from top to bottom [anterior-posterior, left-right, superior-inferior]: [157, 163, 117], [158, 164, 136], [176, 162, 131], [163, 170, 155], [115, 217, 95]), circles: displacement estimated by 2D vessel tracking, crosses: displacement estimated by motion field analysis

The registration was successfully performed on the CT data with and without the lung structure inserted. Fig. 12 shows the overlays of the moving images (A, B, C) and (G, H, I) resp. registered images (D, E, F) and (J, K, L) (magenta) with the fixed images (green) in different planes. In this case 100% IN was chosen as the moving image, because large displacements were expected for this phase. The lung structures are clearly visible as a small assembly of features beneath the skin (only on the right side of the phantom) (A-F). The colors green and magenta indicate displacements of the structures between the two ob-

served phases. The comparison of (A, B, C) and (D, E, F) resp. (G, H, I) and (J, K, L) showed that registration was successful even for the large displacement case for both acquisitions. There was no clear difference in the quality of registration between the images with and the images without structure.

The motion fields generated by the registration process showed movements of the vessel structures of the 100% IN phase with respect to the 0% IN phase (Fig. 13). The direction of the green arrows corresponds to the direction of the displacement and the length of the arrows to the magnitude of the displacement. The displacements were observed for the thorax surface (A, B, D, E) and the diaphragm (C, F) indicated by the long arrows. The target (round structure) in B and E did not show huge changes in position compared to the before mentioned structures. The comparison between the motion fields of the phantom without the structure and of the phantom with the structure showed a few small differences (red arrows). The motion field of the phantom without the structure (A, B, C) suggests some strong motion at a featureless location (A: upper left part, C: upper left part) and almost no motion at other locations (B). This motion behaviour could not be observed in the motion field with the features (D, E, F).

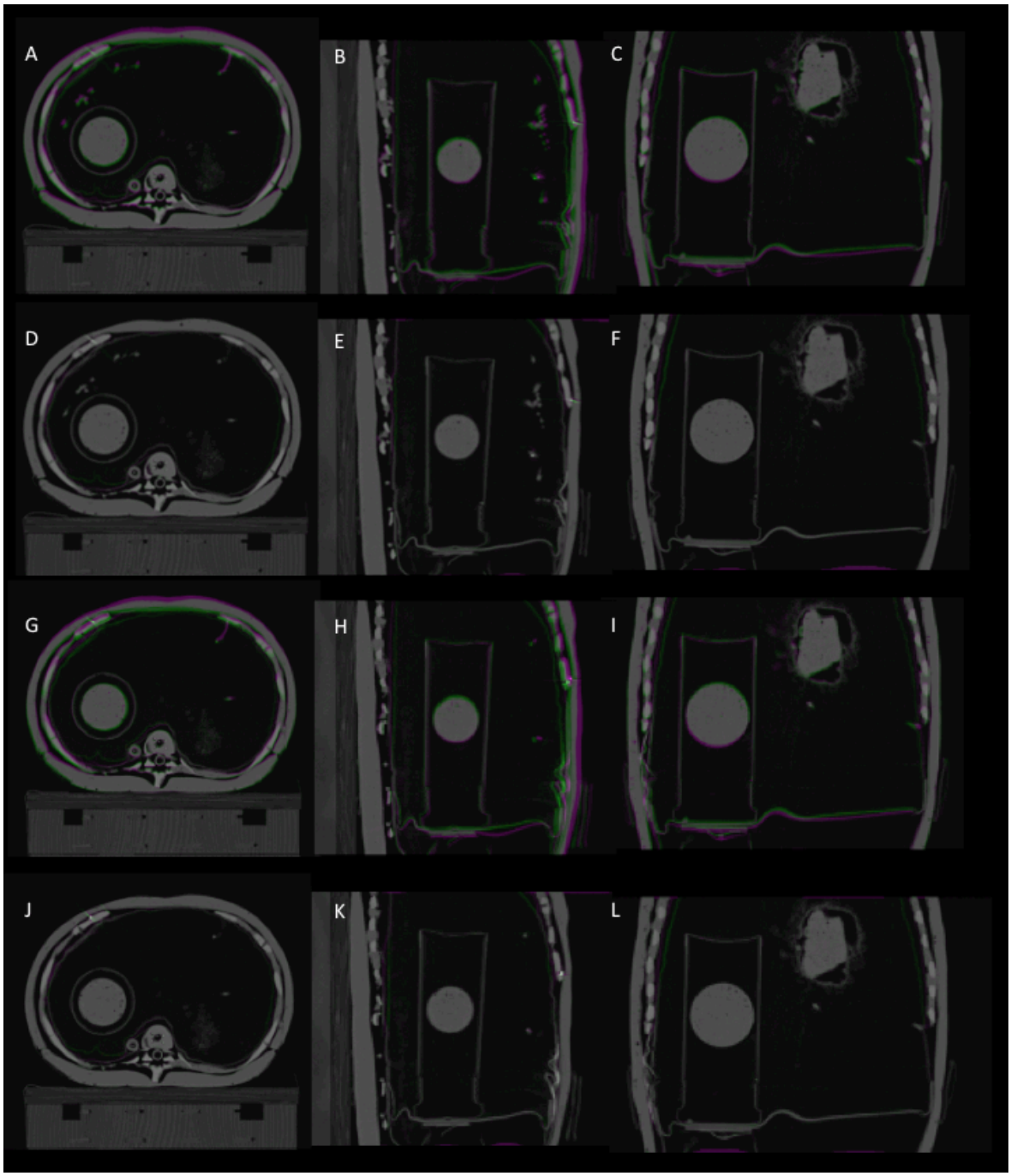

Fig. 12: Registration results: (A, B, C): Overlay of the non-moving image (0% IN) and the moving image (100% IN) with vessel structures, green and magenta are indicating displacements. (D, E, F): Overlay of the non-moving image (0% IN) and the registered image (100% IN) with vessel structures. (G, H, I): Overlay of the non-moving image (0% IN) and the moving image (100% IN) without vessel structures, green and magenta are indicating displacements. (J, K, L): Overlay of the non-moving image (0% IN) and the registered image (100% IN) without vessel structures. (A, D, G, J): Transversal plane, (B, E, H, K): Sagittal plane, (C, F, I, L): Coronal plane.

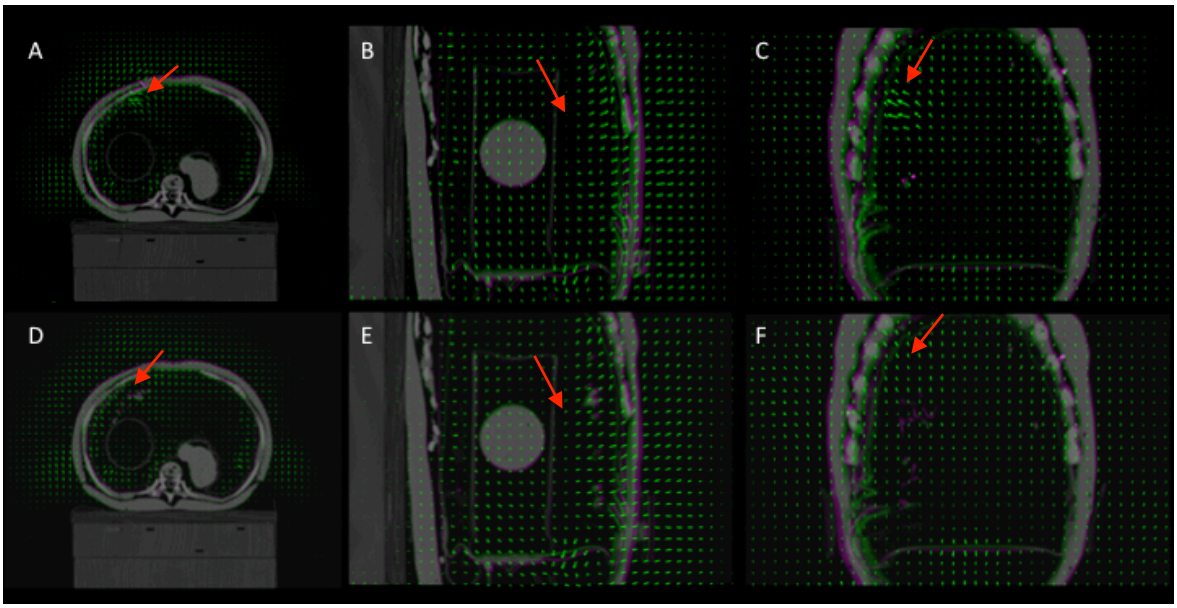

Fig. 13: Displacement fields of the 100% IN phase without (A, B, C) and with structure (D, E, F): The green arrows indicate the displacement in respect to the non-moving image. The red arrows highlight differences. (A, D): Transversal plane, (B, E): Sagittal plane, (C, F): Coronal plane.

3.2.3 Discussion

For the 2D vessel tracking one has to note that the slice thickness was 1 mm, therefore the absolute values especially for the superior-inferior direction should be considered with caution. Another limitation is the technique itself. By just considering a 2D plane and looking for the centroid, one cannot distinguish the total motion of the vessels from changes of the centroid location due to structures moving into the plane from another slice. Such structures from other slices are wrongly interpreted as vessel movement. Nevertheless the estimated motion was in agreement with the motion obtained by the registration process. Therefore one can conclude that the 3D printed lung structure showed motion in the millimeters range, and that the registration could follow the motion.

The motion field from the registration of the phantom with the vessel-like structure looked more reasonable at certain locations. Therefore the structure could be a huge benefit in studies involving deformable image registration (as in this study).

4 Outlook

4.1 Decoupling of the target motion

The next steps will be to design a suitable target holder with a system, which translates the rotational motion of the motor into a linear motion. The target should be able to move approximately 2 cm to provide enough motion for proton beam studies. Also important is the replacement of the current pressure sensor to provide a more appropriate pressure range. The operators of the lung phantom often use pressure values between -3 kPa and 7 kPa. A suitable option would be the SSCDRRN100MDAA5 sensor from Honeywell [17], which operates between -10 kPa and +10 kPa.

4.2 Development of lung structures

Further investigation into other materials with better stability is still required. A good approach would probably be to order samples of different 3D print materials and test if their properties are suitable for lung structures.

Another problem, which still needs to be solved, is the insertion of the lung structure into the lung phantom. For the positioning of the structure within an already existing lung one is most likely forced to cut the foam. A different possibility would be to insert the structure during the manufacturing of the lung, which could, however, be hard to accomplish.

5 Conclusion

This study shows first steps in the development of a system, which should be able to provide decoupled target motion in a lung phantom. It could be shown that the system is able to measure a pressure signal and to move a motor accordingly (even for patient breathing). In the future this system will be further improved to provide a powerful tool to mimic target motion of real patients.

The development of a more realistic lung showed the feasibility of adding additional features, which provided moving structures for deformable image registration. This kind of structure will make the phantom more patient-like than it already is.

As already discussed in chapter 4 further improvements are still necessary. Especially in the implementation of the motor and the choice of the lung material further investigation is needed.

Both developments, the decoupling of the target motion and the more realistic lung, will become very useful for verification and validation of different treatment techniques in the future.

6 Acknowledgements

I would like to thank Prof. Dr. Antony John Lomax who gave me the possibility to do this project at PSI. Special thanks go also to Dr. Giovanni Fattori and Dr. Rosalind Lucy Perrin for their support and guidance during the project. They helped me each time I struggled with problems. In addition I would also like to thank Mr. Pablo Fernandez Carmona and Mr. Harald Alfred Regele for their input and support regarding all electronic issues. To Mr. Viktor Eggspühler go my thanks for his support and advice regarding the 3D printing.

7 References

[1] Bortfeld T, Jiang SB, Rietzel E. Effects of motion on the total dose distribution. Semin Radiat Oncol 2004; 14(1): 41–51 [https://doi.org/10.1053/j.semradonc.2003.10.011][PMID: 14752732]

[2] Bert C, Durante M. Motion in radiotherapy: particle therapy. Phys. Med. Biol. 2011; 56(16): R113-44 [https://doi.org/10.1088/0031-9155/56/16/R01][PMID: 21775795]

[3] Phillips MH, Pedroni E, Blattmann H, Boehringer T, Coray A, Scheib S. Effects of respiratory motion on dose uniformity with a charged particle scanning method. Phys. Med. Biol. 1992; 37(1): 223–33 [https://doi.org/10.1088/0031-9155/37/1/016]

[4] Perrin RL, Zakova M, Peroni M*, et al.* An anthropomorphic breathing phantom of the thorax for testing new motion mitigation techniques for pencil beam scanning proton therapy. Phys. Med. Biol. 2017; 62(6): 2486 [https://doi.org/10.1088/1361-6560/62/6/2486]

[5] Intel Corporation. Intel Edison Kit for Arduino: Hardware Guide; 2017 [cited 2017 June 30] Available from: URL: https://www.intel.com/content/dam/support/us/en/documents/edison/sb/edison-arduino-hardware-guide.pdf.

[6] Panasonic. Datasheet: Pressure Sensor/PS-A (ADP5); August 2015.

[7] Parr A. Hydraulics and Pneumatics: A Technician's and Engineer's Guide. Elsevier Science 2011.

[8] Jones DW. Control of Stepping Motors: A Tutorial: University of Iowa; 1995 [cited 2017 June 6] Available from: URL: http://homepage.divms.uiowa.edu/~jones/step/.

[9] CrustCrawler Inc. MX-28R Technical Reference Guide; June 2012.

[10] ROBOTIS CO. User's Manual RX-28.

[11] ITEAD STUDIO. Datasheet: MAX485 Module; July 2013.

[12] Bircher W., Leddy M. Dynamixel RX-28, RS-485 & Arduino [cited 2017 May 16] Available from: URL: https://smartgrasp.wordpress.com/dynamixel-rx-28-rs-485-arduino/.

[13] savelectronics. Dynamixel for Arduino [cited 2017 May 17] Available from: URL: https://sourceforge.net/projects/dynamixelforarduino/files/?source=navbar.

[14] Seeed Technology Inc. Grove_LCD_RGB_Backlight [cited 2017 May 17] Available from: URL: https://github.com/Seeed-Studio/Grove_LCD_RGB_Backlight.

[15] 3D SYSTEMS. VisiJet M2 Materials; March 2017.

[16] Bikis Christos. Investigation into the dynamic properties and optimization of the MRI lung insert of LuCa breathing phantom. bachelor thesisETH 2014 Dec 7.

[17] Honeywell. Datasheet: TruStability Board Mount Pressure Sensores: SCC Series-Standard Accuracy, Compensated/Amplified; August 2014.